Detailed analysis of radiative transitions from defects in *n*-type monocrystalline silicon using temperature- and light intensity-dependent spectral Photoluminescence

Robert (μRob) Lee Chin [*], Michael Pollard, Yan Zhu, Ziv Hameiri

School of Photovoltaics and Renewable Energy Engineering, University of New South Wales, Sydney, Australia

A B S T R A C T

Sub-bandgap luminescence is characteristic of radiative transitions from defects in semiconductors. However, methods to extract defect-identifying parameters from this luminescence are lacking. Here, we present a method to extract these parameters from temperature- and intensity-dependent micro-photoluminescence (μPL) spectra. The initial "coarse" analysis determines the relevant radiative recombination mechanism by fitting the integrated defect PL spectra with phenomenological models for the temperature- and intensity-dependence. The subsequent "detailed" analysis fits the integrated defect PL spectra using rigorous physical models for the defect radiative recombination and spectral line-shape. Finally, defect parameters are extracted, including the defect energy level(s). As we obtain these values directly from the defect luminescence, our method provides higher confidence than more traditional indirect methods, such as those involving band-to-band PL and photoconductance. We demonstrate our method on spatially non-uniform defects with radiative transitions in *n*-type monocrystalline silicon samples. It is shown that the defect PL originates from the donor-acceptor pair recombination mechanism, involving a shallow acceptor and deeper donor energy level. The acceptor level is extracted from the temperature-dependent spectra, whilst the intensity-dependent spectra give the sum of acceptor and donor energies.

1. Introduction

The photoluminescence (PL) of semiconductors, including crystalline silicon, is emitted as a spectrum of photon energies [1] The room-temperature PL spectra of high-quality float-zone (FZ) silicon is a broad, asymmetric band with maximum intensity at approximately 1.09 eV, close to the indirect band-gap of silicon (1.12 eV) [2] On a logarithmic scale, multiple shoulder peaks are also observed; these are due to optical emission via phonon absorption and phonon emission [3] Collectively, these PL peaks are the band-to-band spectral PL (PL_BB). Each peak can physically be described by [4].

$$dr_{sp}(h\nu) \propto \left[h\nu - \left(E_g \pm \hbar\omega\right)\right]^2 \times \exp\left[-\frac{h\nu - \left(E_g \pm \hbar\omega\right)}{k_B T}\right] \qquad 1$$

where dr_{sp} is the spontaneous rate of emission, $h\nu$ is the photon energy, E_g is the silicon band-gap energy, $\hbar\omega$ is the phonon energy with the positive (negative) sign denoting phonon emission (absorption) and $k_B T$ is the thermal energy. The quadratic term accounts for the density of states in the conduction and valence band. The exponential term is related to the occupation probability of states in the valence and conduction band. This term is known as the Maxwell-Boltzmann distribution and is responsible for thermal broadening of the spectral line-shape

[4].

Silicon feedstock for photovoltaic devices contains a variety of impurities, typically unwanted [5] These impurities may decrease the minority carrier lifetime by acting as effective centres for non-radiative recombination [6,7] The recombination activity of these defects can be quantified by measuring the spectrally-integrated PL_BB [8], which, roughly speaking, is directly proportional to the effective lifetime (τ_{eff}). A disadvantage of relying on PL_BB is that it is an indirect method to probe defects – multiple defect levels may influence PL_BB, making it difficult to probe specific defect levels. Some defects in silicon, most notably dislocations [9–13], oxide precipitates [9,12,14] and thermal donors [15, 16], introduce additional PL peaks occurring at specific *sub-bandgap* energies [1,17] In this paper, we collectively denote these peaks as PL_defect. Using PL_defect to study specific radiative defects avoids the issues posed by using PL_BB. Decoration of dislocations or precipitates with impurities has been found to modify the nature of PL_defect [18] For example, dislocations in silicon measured at 80 K possess four distinct PL_defect peaks; D1, D2, D3 and D4 at energies 0.807 eV, 0.870 eV, 0.935 eV and 1.0 eV, respectively [19] The D1 and D2 lines are modulated when the dislocations are decorated with impurities, such as oxygen precipitates [15,20,21,21,22] As the PL_defect peaks are spectrally resolved and therefore distinguishable from the PL_BB peaks, the defect

---

* Corresponding author.
  E-mail address: r.leechin@student.unsw.edu.au (R.(μL. Chin).

parameters underlying the defect PL can be studied in isolation from any other recombination mechanisms. It is important to note that understanding the nature of the radiative transition defects may be limited by the fact that they typically are not the dominant recombination active species in silicon wafers.

Quantitative analysis of PL$_{defect}$ requires first identifying the underlying recombination mechanism. In crystalline semiconductors under relatively low irradiance (0.1–10 W/cm^2), there are at least four distinct radiative recombination mechanisms [4] Hence, it is instructive to have a brief overview of these mechanisms in terms of their spectral behaviour as a function of temperature and light intensity.

1.1. Neutral-donor (acceptor) bound excitons, D^0-X (A^0-X)

An exciton is formed by an electron (hole) at a donor (acceptor) level and a hole (electron) in the valence (conduction) band. The light-intensity dependence is super-linear with exponent between one and two [23] The emitted photon energy is equal to the bandgap energy minus both the free-exciton binding energy (14.3 meV) and the binding energy of an exciton at the defect level (E_{BX}). The latter is linearly proportional to the defect binding energy [4] The line-shape does not have a generalized equation, but is narrow at low temperature and becomes thermally-broadened with increased temperature [24].

1.2. Ionized-donor (acceptor) bound excitons D^+-X (A^--X)

An electron (hole) at a donor (acceptor) level recombines with a hole (electron) in the valence (conduction) band. This mechanism has similar behaviour to the D^0-X (A^0-X) processes. However, its existence is dependent on the electron-to-hole effective mass ratio (σ) of the semiconductor [4] In silicon, the value of σ is such that this radiative recombination mechanism is non-existent [4] In materials with effective mass ratio conducive to this process, the energy position of D^0-X (A^0-X) and D^+-X (A^--X) peaks follows a particular ordering depending on the value of σ [25].

1.3. Donor-acceptor pair (D^0-A^0)

If both donors and acceptors are present, there is a probability of tunneling recombination between a neutral donor and a neutral acceptor [26] The donor and acceptor can be considered as a single defect pair. The inter-level recombination event ionizes both levels (D^+-A^-) and emits a photon with energy equal to the energy separation between the donor and acceptor level, plus an additional Coulombic term accounting for the creation of the charged pair [26]. We denote this recombination mechanism as DAP recombination.

A key feature of D^0-A^0 recombination is a blue-shift of the peak emission energy with increasing *irradiance* [26] This blue-shift occurs as a result of Coulombic interaction between pairs increasing the emitted photon energy [26] At higher irradiance (higher injection), the pairs are more closely spaced; hence, the larger Coulombic interaction and blue-shift. The excitation-dependence is sub-linear [23] For very close-pairs, sharp, high-intensity peaks may appear due to the Coulombic interaction [24] This emission depends on the pair concentration and appears to be quite rare in silicon [4] The more distant pairs form a continuous, lower-intensity but broad spectra, which is more commonly observed than the sharp peaks [4] The spectral line-shape is non-trivial, but various models exist to describe it [27,28].

This recombination mechanism has previously been observed in compensated silicon [24,29].

1.4. Free electron and neutral acceptor, free hole neutral donor (e-A^0, h-D^0)

A free electron (hole) recombines with a neutral shallow acceptor (donor). The emitted photon energy is equal to the difference between the band-gap energy and the acceptor (donor) ionization energy [4] The excitation-dependence is sub-linear [23] The spectral line-shape follows the Maxwell-Boltzmann distribution due to the free electron (hole). For an indirect semiconductor it is given by [4].

$$\text{PL}_{e-A^0(h-A^0)}(h\nu) \propto \left[h\nu - \left(E_g - E_{a(d)} \right) \right]^2 \exp\left[-\frac{h\nu - \left(E_g - E_{a(d)} \right)}{k_B T} \right] \qquad 2$$

Fig. 1 shows the band-diagram for each recombination mechanism and Table 1. Summarises the features of each mechanism.

Spectral PL can be combined with a confocal micro-PL (μPL) detection approach to probe the recombination parameters of *spatially non-uniform* defects [30–34] In this detection approach, the sample is optically excited with focused monochromatic light, resulting in PL [35–37] The PL emission to be measured passes through a confocal pinhole to eliminate the out-of-focus background signal and therefore localise the detection volume to the vicinity of the excitation volume centre [38] This localised detection method is particularly advantageous for probing non-uniform defects compared to large-area detection methods such as quasi steady-state PL (QSSPL) [39] and quasi steady-state photoconductance (QSSPC) [40], which are more affected by spatial non-uniformities in the bulk lifetime [41] The confocal spectral μPL arrangement has previously been used for many studies, including probing D-lines in multi-crystalline silicon wafers [19,33,35,42,43], the doping profiles of heavily doped layers in solar cells [31], and for microscopic transient carrier lifetime [37,44].

Defect PL is typically studied via temperature- and intensity-dependent measurements [13,30] The temperature-dependence can be used to extract a defect activation energy, which is often interpreted as the defect energy level, relative to one of the band-edges [45] The power-law intensity-dependence is commonly used to determine the radiative recombination mechanism [23] This analysis does not take into consideration the excess carrier density, which is important if measurements are in the high-injection regime. This is entirely possible for silicon at light intensities of several Suns or more. For example, a typical 180 μm, *p*-type wafer doped at 10^{15} cm^{-3} with effective lifetime of 100 μs will have an average excess carrier density of 7.7×10^{15} cm^{-3} under 3-Sun irradiance. This represents a relative error of approximately 7x compared to assuming low-injection, i.e. using the approximation $np - n_i^2 \approx N_{dop}\Delta n$ compared to the full expression $np - n_i^2 = \Delta n^2 + N_{dop}\Delta n$, where Δn is the excess carrier concentration and N_{dop} is the doping density.

Here, we present a method to analyze radiative defects from temperature- and intensity-dependant spectral PL. This method consists of two steps: the "coarse" analysis typically used for these measurements, as described above, followed by a "detailed" analysis taking into consideration the injection-dependence of the defect's radiative recombination mechanism.
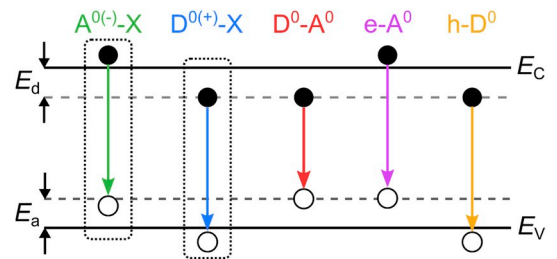

Fig. 1. *Energy-band diagram of defect-related radiative transitions in a semiconductor. E_V and E_C represent the valence and conduction band-edges, respectively. E_d and E_a represent the depth of the acceptor and donor levels from their respective band-edges. D^+-X and A^--X transitions are shown for completeness, although, it is emphasized that they cannot occur in silicon. Filled circles represent electrons and open circles represent holes. The dotted rectangles represent bound-excitons. (For interpretation of the references to color in this figure legend, the reader is referred to the Web version of this article.)*

Table 1

Characteristic features of silicon-related radiative defect recombination mechanism.

Characteristic	Mechanism		
	$D^{0(+)}$-X, $A^{0(-)}$-X	D^0-A^0	e-A^0, h-A^0
Spectral Line-shape	Narrow	Complex – depends on spatial distribution of the pairs.	Maxwell-Boltzmann – asymmetric and broadens with temperature.
Excitation-Dependence	Super-linear	Sub-linear	Sub-linear
Additional Features		Peak emission energy blue-shifts with increasing excitation.	

2. Experimental methods

To characterize PL_{defect}, *n*-type monocrystalline samples were selected. These samples were known to develop non-uniform bulk defects after annealing, similar to the well-known oxygen ring precipitates in Czochralski silicon, which also have defect PL [46] The non-uniform defects make these samples good candidates to demonstrate the μPL-based approach.

2.1. Characterization techniques

2.1.1. PL imaging and photoconductance lifetime

Room-temperature PL images were measured using a PL imaging system (BTi LIS-R1). The PL images were deconvolved with the point-spread function (PSF) of the imaging camera which accounted for the scattering of the PL photons within the camera sensor [47] This significantly improved the spatial resolution of the PL images.

Injection-dependent lifetime curves were measured using a commercial PC-based system (Sinton WCT-120) at 30 °C. The wafers were centered on the PC coil sensor region and the system was used in the generalized analysis mode [40] The wafer dark conductivity was used to determine the bulk doping concentration. Samples were surface passivated as described in Section B.

2.1.2. Optical reflectance and transmittance

The optical reflectance and transmittance within the same range as the spectral BB PL were measured using a PerkinElmer spectrophotometer (model Lambda 1050 UV/Vis/NIR). This was used to model photon re-absorption effects for calibrating the excess carrier density.

2.1.3. Spectral PL

Spectral PL were measured using a customized Nikon Eclipse microscope (see Fig. 2). Excitation was provided by a 660 nm light-emitting diode (LED) passing through a 50-50 beam-splitter and focused on the sample using a reflective objective with 15 × magnification and 0.5 numerical aperture (NA). The excitation spot size on the sample was 1.428 mm for all measurements. The samples were placed inside a temperature-controlled cryostat stage with a temperature range from 77 K (−196 °C) to 693 K (420 °C) with temperature resolution of 0.1 °C. Thermal paste with thermal conductivity of 8.9 W/mK was applied to the sample side contacting the stage to improve the thermal coupling between the sample and the cryogenic stage. The PL signal was filtered from the reflected excitation using an optical-density (OD)-4900 nm long-pass (LP) interference filter. The PL signal was coupled into a 550 μm, 0.22 NA multi-mode optical fiber and detected using an indium-gallium arsenide (InGaAs) imaging spectrometer with detection range from 900 nm (1.38 eV) to 1700 nm (0.73 eV), spectral resolution of 1.66 nm, and 16-bit dynamic range. All spectral measurements are measured with a 1 s integration period, using the average of 100 measurements to improve the signal-to-noise (SNR) ratio by a factor of ten. All spectra
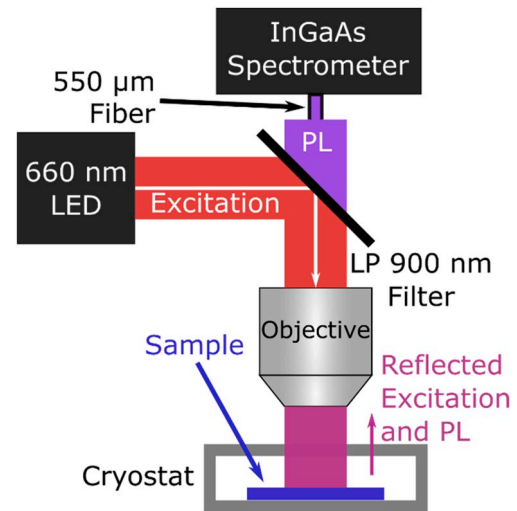

Fig. 2. μPL setup for spectral PL measurements.

were corrected for the quantum efficiency/spectral response of the optical detection system (spectrometer and objectives). This was achieved by heating the cryogenic stage to 670 K (400 °C) and curve fitting the measured blackbody spectra against the theoretical blackbody spectra [48] Spectra were also corrected for the non-uniform wavelength interval. As the PL intensity is defined normalized to a constant wavelength interval and in practice the spectrometer does not have a constant wavelength interval, this must be corrected for by dividing the PL intensities by the wavelength interval. In addition, spectra were corrected accounting for the fact that the spectra are measured as a function of emission wavelength, but analyzed in terms of emission energy. This means the spectra must be divided by a factor of E^2 where E is the emission energy [49].

Temperature-dependent spectral PL (TDS-PL) was measured by varying the stage temperature from 80 K to 300 K in steps of 10 K. At each temperature step, the PL spectra were measured. Sufficient time was allowed between temperature steps to ensure the stage temperature stabilized to within 0.1 K of the set temperature. The light irradiance was kept constant at approximately 19.5 Suns (1950 mW/cm²). In this work, we emphasize that we define 1 Sun as 100 mW/cm², despite the monochromatic excitation.

Irradiance-dependent spectral PL (IDS-PL) were measured over approximately one order magnitude of irradiance by varying the excitation LED current from 100 mA (1.95 Suns, 195 mW/cm²) to 1200 mA (19.5 Suns, 1950 mW/cm²) in increments of 100 mA. At each irradiance step the stage temperature was kept constant at 80 K while the PL spectra were measured.

To confirm that the sample temperature was equal to the stage temperature, the main peak of the spectral PL_{BB} (TO⁻ phonon) measured at the minimum temperature of 80 K was fitted according to a physical model for the PL_{BB} peak [50] A best-fit temperature of 79.5 ± 0.9 K was determined, justifying the assumption that the sample temperature is equal to the stage temperature (Fig. 2).

2.2. Sample processing

Samples are commercial double-side polished phosphorus-doped monocrystalline silicon wafers with a measured bulk resistivity of 2.4 Ω.cm, thickness of 525 μm, and a diameter of 4 inches. The wafer was cleaved into quarters. The interstitial oxygen concentration ([O_i]) was approximately 15 ppma (7.5×10^{17} cm⁻³), as measured by Fourier-transform infrared spectroscopy (FTIR) [51] The samples were Radio Corporation of America (RCA) cleaned [52], followed by surface passivation with plasma-enhanced chemical vapor deposition silicon

nitride (PECVD SiN$_x$) on both sides of the wafer [53] The SiN$_x$ deposition temperature was 400°C and the SiN$_x$ thickness is 65 nm with refractive index of 2.05 [54] The passivation quality was assessed by QSSPC lifetime, while the bulk quality was determined by both QSSPC-based lifetime measurements and PL imaging (BTi LIS-R1). It was determined that bulk defects limited the bulk lifetime to approximately 100 µs, as the surface passivation recipe used typically provides surface lifetimes an order of magnitude larger than the measured effective lifetime. Low-temperature µPL was used to measure the PL spectra; no radiative defects were observed (see more details regarding the characterization techniques above).

The SiN$_x$ was then etched using a weak hydrofluoric (HF, 5%) solution before dipping the samples in a HF (49%):nitric acid (1:10) solution for a few minutes to etch around 5 µm from each surface. This ensured that no SiN$_x$ and native oxide were present on the wafer prior to surface passivation. The wafers were RCA cleaned again before being subjected to an extended annealing process in an oxygen ambient in order to activate bulk defects. The temperature profile was as follows: 45 min ramp-up to the annealing temperature of 925 °C, followed by 3 h annealing at 925 °C, and finally a 45 min ramp-down to room-temperature. The annealed wafers were then RCA cleaned, followed by surface passivation with PECVD SiN$_x$ using the same recipe as the pre-anneal step. Samples were then characterized as described below.

2.3. Analysis methods

Analysis can be divided into two main steps:

1) *Recombination mechanics*: PL imaging and QSSPC lifetime. Determination of the radiative recombination mechanism responsible for the defect PL based on empirical observations of the spectral line-shape, peak position and spectral integral with respect to temperature and light intensity.
2) *Defect parameterization*: Use of appropriate radiative recombination models to analyze the defect PL. Extraction of defect parameters including the defect energy levels.

For the second step, knowledge of the excess carrier densities and defect PL recombination rates are required, as defect recombination rates are expected to be temperature- *and* injection-dependent. Methods to calculate excess carrier densities and recombination rates are detailed as following.

2.3.1. Calibrating the band-to-band PL to average excess carrier densities

The spectrally-integrated PL$_{BB}$ is intimately related to the excess carrier density (Δn) [55].

$$PL_{BB} = A_i B_{rad} \Delta n (\Delta n + N_{d,ion}) \qquad\qquad 3$$

where B_{rad} is the radiative recombination coefficient [56], and $N_{d,ion}$ is the ionized dopant concentration. Note that B_{rad} is a function of both temperature and excess carrier density [56,57] A_i is a system- and sample-dependent calibration constant that must be known in order to calculate Δn [58].

Photons emitted inside the silicon bulk due to radiative recombination can be *re-absorbed* as they propagate towards the detector, resulting in an emission-energy-dependent attenuation of the spectral PL known as *photon re-absorption* [38,58] At temperatures greater than approximately 300 K, this effect is strongly influenced by the carrier profiles within the wafer [59] Hence, modelling of the PL$_{BB}$ spectra can be used to determine Δn, which can then be used to determine A_i and hence calculate Δn for future measurements.

Considering photon re-absorption, the spectral PL$_{BB}$ is proportional to the volume integral of the rate of spontaneous band-to-band emission (dr_{sp}) weighted with a photon reabsorption factor (f_{reab}) [38].

$$PL_{BB}(h\nu) = k \int_0^W f_{reab}(h\nu, z) \times dr_{sp}(h\nu, z) \, dz \qquad\qquad 4$$

where k is the proportionality constant relating PL$_{BB}$ (photons.s^{-1}) to dr_{sp} (photons.s^{-1}.eV^{-1}.cm^{-3}). The ordinates $h\nu$ and z are the photon energy and depth into the wafer, respectively, while the integration is performed over the wafer thickness (W). dr_{sp} is defined as [60].

$$dr_{sp}(h\nu, z) = \frac{\alpha_{\{BB\}} \times (h\nu)^2}{4\pi^3 c^2 \hbar^3} \frac{1}{\exp\left(\frac{h\nu - \Delta\mu(z)}{k_B T}\right) - 1} \, d(h\nu) \qquad\qquad 5$$

where $\alpha_{\{BB\}}$ is the band-to-band absorption coefficient, c is the speed of light in vacuum, $\hbar$ is the reduced Planks's constant and $k_B T$ is the thermal energy. $\Delta\mu(z)$ is the chemical potential of photons, defined as:

$$\Delta\mu(z) = k_B T \ln\left(\frac{n(z) \times p(z)}{n_i^2}\right) \qquad\qquad 6$$

where n_i is the intrinsic carrier concentration, and $n(z)$ and $p(z)$ are the electron and hole profiles, respectively.

For planar wafers, as used in this study and front-side detectionthe photon-reabsorption factor $\gamma(h\nu, z)$ is [58].

$$\gamma(h\nu, z) = T_F \frac{exp(-\alpha z) + R_F \, exp(-\alpha[2W - z])}{1 - R_F R_B \, exp(-2\alpha W)} \qquad\qquad 7$$

where T_F is the front-surface transmittance and R_F and R_B are the front and back surface reflectance, respectively. Note that this model does not account for photons travelling at an angle to the z-axis.

To model the PL$_{BB}$ spectra, several quantities are required:

1) *Band-edge absorption coefficient*: This should be at the same temperature as the measured spectral PL$_{BB}$. In this study a "high" temperature of 300 K is used and the absorption coefficient data for crystalline silicon at this temperature is reproduced from Hieu et al. [61].
2) *Optical properties of the wafer*: T_F, R_F and R_B within the same energy range as the spectral PL$_{BB}$.
3) *Carrier profile inside the wafer*: This is calculated numerically using PC1D. The light intensity, excitation wavelength, wafer thickness, wafer doping, temperature and the surface recombination parameter (extracted from the wafer QSSPC lifetime in high-injection, pre-anneal with same surface passivation recipe) are input parameters. The bulk lifetime is used as the independent variable to fit the PL$_{BB}$. Once a good fit is achieved, Δn can be extracted.

An example of this calibration procedure is shown in Fig. 3. Based on the fit, a bulk lifetime of 15 µs was determined. Lifetimes of 1 us, 30 us and 100 us are shown for comparison. For the particular calibration curve ($\tau_{bulk} = 15 \, \mu s$), the absolute relative errors for Δn are 50%, 10% and 20%, respectively. Note that the photon-reabsorption effects are significant only when the absorption coefficient reaches the inverse of the wafer thickness (20 cm^{-1}) [38,59], hence the fitting is weighted towards the high energy tail of the spectral PL$_{BB}$ (1.2 eV–1.4 eV).

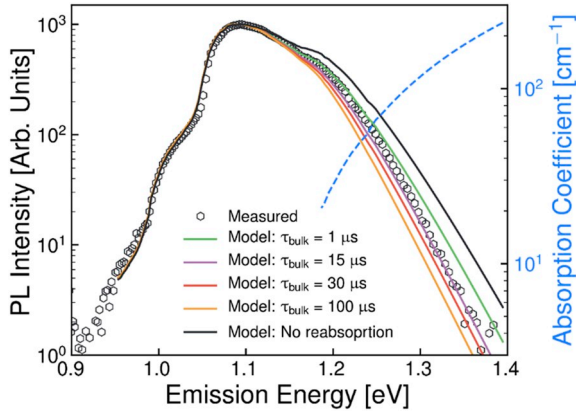We calculate a weighted-average value of Δn ($\overline{\Delta n}$) using the intensity-weighted approach developed by Heinz [37].

$$\overline{\Delta n} = \int_0^W \frac{PL_{BB}(z)}{\int_0^W PL_{BB}(z) dz} \Delta n(z) \, dz \qquad\qquad 8$$

For *n*-type material, $\Delta n(z) \approx p(z)$ and the term PL$_{BB}(z)$ is the local BB radiative recombination rate..

Eq. (8) assumes that Δn does not vary radially along the cylindrical

Fig. 3. Comparison of measured spectral PL_{BB} and the modelled spectral PL_{BB}. Note that only $\tau_{bulk} = 15\ \mu s$ gives an adequate fit; the other spectra are shown for comparison of sensitivity. The dashed blue line on the secondary y-axis represents the absorption coefficient in the range relevant for significant photon re-absorption. (For interpretation of the references to color in this figure legend, the reader is referred to the Web version of this article.)

detection volume. This is a reasonable assumption when the collection spot-size is at least several times smaller than the excitation spot-size. In our setup, we employ large-volume excitation and relatively localized detection. The excitation spot size (full-width at half-maximum) obtained using optical imaging is 1428 μm. The collection spot size ($1/e^2$) determined using the knife-edge technique [62] is 306 μm; approximately five times smaller than the excitation spot-size. Therefore, the assumption that lateral variations in Δn *do not* significantly influence the PL signal is justified and the use of Eq. (8) is appropriate.

The calibration factor may be written as the product of a temperature- and light-intensity dependent reabsorption-factor term ($f_{reab}(T, \phi)$) and a system-dependent term ($A_{i,sys}$) [58].

$$A_i = A_{i,sys} f_{reab}(T, \phi) \qquad 9$$

$A_{i,sys}$ is expressed as [58].

$$A_{i,sys} = \frac{\int \int_0^W dr_{sp}(h\nu, z)\ dz d(h\nu)}{B_{rad}(\Delta n)\overline{\Delta n}(\overline{\Delta n} + N_{dop})} \qquad 10$$

$f_{reab}(T, \phi)$ is given by:

$$f_{reab}(T, \phi) = \frac{\int_0^W f_{reab}(h\nu, z) \times dr_{sp}(h\nu, z)\ dz}{\int_0^W dr_{sp}(h\nu, z)\ dz} \qquad 11$$

Note that in Eq. (11), the term $dr_{sp}(h\nu, z)$ is temperature-dependent due to the temperature-dependence of the absorption coefficient.

$\int_0^W dr_{sp}(h\nu, z)\ dz$ represents the spectral PL_{BB} corrected for photon reabsorption and scaled to match the measured spectral PL_{BB}. Thus, all other $\overline{\Delta n}$ at different T and irradiance (ϕ) can be calculated by solving Eq. (3) substituting $\Delta n = \overline{\Delta n}$:

$$\overline{\Delta n}(T, \phi) = -\frac{N_{dop,ion}}{2} + \sqrt{\left(\frac{N_{dop,ion}}{2}\right)^2 + \frac{1}{A_{i,sys} \times f_{reab}(T, \phi)} \frac{\int PL_{BB}(T, \phi)\ d(h\nu)}{B_{rad}}} \qquad 12$$

Note $N_{d,ion}(T)$ is the ionized dopant concentration, which varies as a function of temperature [63] Note that Eq. (12) must be calculated iteratively, as B_{rad} is a function of $\overline{\Delta n}$ [56,57] The low-injection value of B_{rad} is the initial guess.

2.4. Converting defect PL to defect PL recombination rates

Spectrally-integrated defect PL ($\int PL_{defect}\ d(h\nu)$) are converted into defect recombination rates (R_{defect}) by multiplying by a calibration factor (k):

$$R_{defect} = k \times \int PL_{defect}\ d(h\nu) \qquad 13$$

γ is calculated from the ratio of the measured spectrally-integrated PL_{BB} ($\int PL_{BB}\ d(h\nu)$) and the true PL_{BB} recombination rate, determined using the calculated $\overline{\Delta n}$:

$$\gamma = \frac{B_{rad}(\overline{\Delta n})\overline{\Delta n}(\overline{\Delta n} + N_{dop,ion})}{\int PL_{BB}\ d(h\nu)} \qquad 14$$

### 3. Results and discussion

3.1. Recombination mechanics

3.1.1. PL imaging and photoconductance lifetime

Fig. 4 shows the room-temperature PL image of the monocrystalline wafer quarter, after the annealing and re-passivation. Concentric, bright-dark striations are observed with decreased PL counts (increasing recombination) towards the radial origin. These striations are attributed to non-uniform concentrations of bulk defects. One possibility for the defects is oxygen precipitates, which often appear as striation or ring patterns [64] A similar halo-like pattern has been observed for thermally-activated defects in n-type FZ silicon [65] Due to the strong non-uniformity in the PL intensity, we selected representative "Bright" and "Dark" locations on the sample for spectral PL measurements.

The QSSPC lifetime is shown in Fig. 5. We propose two main possibilities. The first is that there are two independent defect levels, with one level dominating the effective lifetime. This was determined using the parameterization by Murphy et al. [66,67], wherein the intrinsic-lifetime ($\tau_{intrinsic}$)-corrected effective lifetime, denoted the residual lifetime ($\tau_{residual} = [\tau_{bulk}^{-1} - \tau_{intrinsic}^{-1}]^{-1}$) is plotted as a function of ratio (X) of the the minority carriers (Δp) to the majority carrier concentration (n). Each independent defect level – denoted "τ_A" and "τ_B", respectively – can be fitted with a linear function. The total residual lifetime is the inverse sum of the inverse lifetimes [66,68,69].
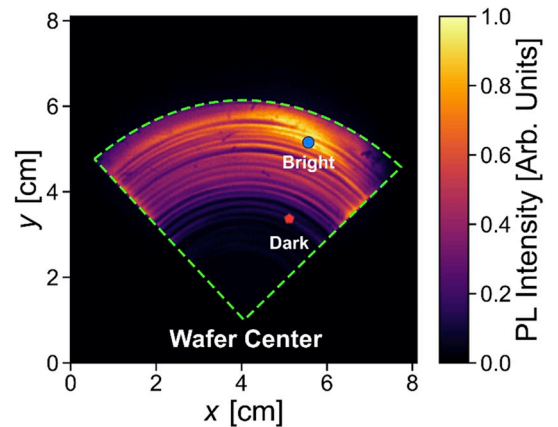
Fig. 4. Room-temperature PL image of the monocrystalline wafer. The edge of the wafer quarter is highlighted by the dashed green line. The approximate "Bright" and "Dark" locations are indicated by the blue circle and red pentagon, respectively. The PL intensity is normalized to the maximum intensity across the wafer. (For interpretation of the references to color in this figure legend, the reader is referred to the Web version of this article.)
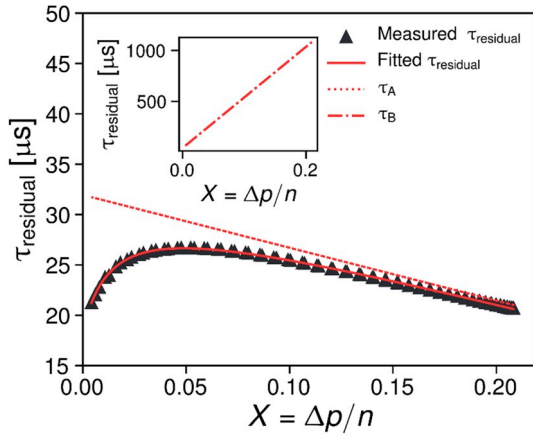
Fig. 5. $\tau_{residual}$ vs. X. The solid red line is the fitted residual lifetime and the dotted and dot-dashed (inset) line represent the lifetime for the two independent defect levels, denoted "A" and "B", respectively. (For interpretation of the references to color in this figure legend, the reader is referred to the Web version of this article.)

$$\frac{1}{\tau_{residual}} = \frac{1}{\tau_A} + \frac{1}{\tau_B} \tag{15}$$

A second possibility is that the defect concentration is highly non-uniform [70] Regardless, even at the maximum light intensity of approximately 75 Suns, the sample remains in low-injection. To be in high-injection, it is assumed $\Delta n > 10 N_d$, where N_d is the bulk doping density. In our measurement, the maximum value of X is 0.21. Knowing $X = \frac{p}{n} = \frac{\Delta n}{\Delta n + N_d} = \frac{1}{1 + \frac{N_d}{\Delta n}}$ leads to the expression $\Delta n = \frac{1}{\frac{1}{X} - 1} N_d$. This gives $\Delta n = 0.27 N_d$, meaning that the sample's maximum injection is still in the low-injection regime. Hence, we could not estimate J_0 from this measurement, as this requires lifetime data in the high-injection regime.

We estimate J_0 of 40 fA/cm^2 per side based on the Kane-Swanson method applied to QSSPC lifetime measurements of the same wafer prior to the defect-creating anneal, which was surface-passivated using the same SiN$_x$ recipe. As $\tau_{residual}$ is within 25 μs, it is assumed that the surface recombination is negligible compared to bulk recombination, meaning that the effective lifetime is dominated by bulk recombination ($\tau_{bulk} \approx \tau_{eff}$). We calculated 0.27% error based on the estimated J_0, hence the assumption of $\tau_{bulk} \approx \tau_{eff}$ is well justified.

3.1.2. Temperature-dependent spectral PL (TDSPL)

Fig. 6 shows the temperature-dependent spectral PL inside the "Bright" and "Dark" locations, respectively. Each PL$_{defect}$ peak was fitted using the Voigt function, which represents a phenomenological model for fitting luminescence spectra [71] Based on the relatively symmetric line-shape of each PL$_{defect}$ peak, we rule out the possibility of PL$_{defect}$ arising from transitions involving one or more free-carriers, including e-A^0 and h-D^0 recombination, whose line-shape is asymmetric as detailed in the Introduction.

For the "Bright" location, as the temperature is reduced, the magnitude of the PL$_{BB}$ peaks is slowly reduced in magnitude and the linewidth narrowed. At 200 K, a broad and weak, PL$_{defect}$ peak centered at 0.8 eV becomes visible (cannot be observed at 300 K). As temperature is further reduced, this PL$_{defect}$ peak increases in magnitude and becomes distinct. The peak energy is blue-shifted to 0.92 eV at 80 K. Meanwhile, the PL$_{BB}$ peaks slowly decrease.

Inside the "Dark" location, we observe a single PL$_{defect}$ peak at room temperature. This PL$_{defect}$ peak is centered at 0.786 eV. As the temperature is reduced, this PL$_{defect}$ peak increases in magnitude and becomes blue-shifted. At 210 K, a second shoulder peak on the high-energy side of the main PL$_{defect}$ peak emerges; the main peak is at 0.823 eV while the shoulder peak is 30 meV higher at 0.853 eV. We denote the main and
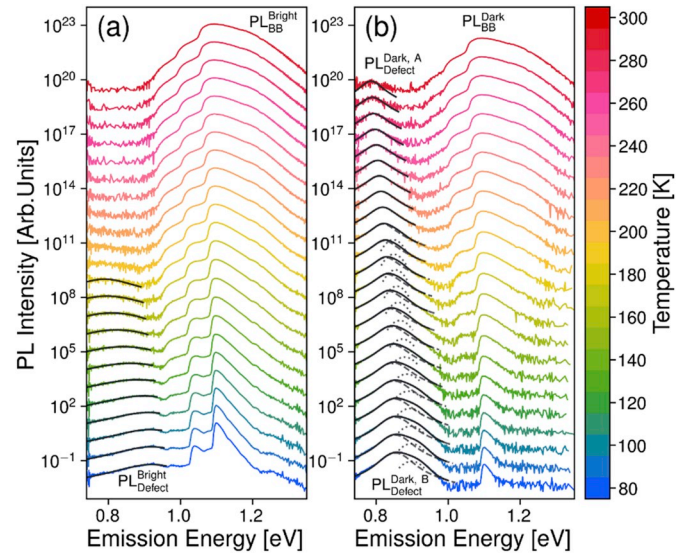
Fig. 6. TDSPL for (a) Bright and (b) Dark locations. All spectra are measured at an excitation light intensity of 19.5 Suns. Spectra are color-coded to temperature, indicated by the color-bar. The spectra are vertically offset for clarity. The fitted defect PL spectra are indicated by the black lines and the individual defect PL components are shown in dashed and dotted gray. (For interpretation of the references to color in this figure legend, the reader is referred to the Web version of this article.)

shoulder peaks "A" and "B", respectively. As the temperature is further reduced, both PL$_{defect}$ peaks increase in magnitude. At 80 K, the main and shoulder PL$_{defect}$ peaks are blue-shifted to 0.854 eV and 0.898 eV, respectively. Similar to the "Bright" region, the PL$_{BB}$ peak steadily decreases in magnitude as the temperature is reduced (at room temperature it is approximately 200 counts higher than PL$_{defect}$).

For both locations, the inverse relationship between the PL$_{BB}$ and PL$_{defect}$ with temperature may imply that the PL$_{defect}$ is associated with highly recombination-active defects.

3.1.3. Phenomenological model for extracting defect energies

The temperature-dependence of PL$_{defect}$ is commonly fitted using an Arrhenius-equation, in order to extract the defect activation energies [30,45,72].

$$PL_{defect}(T) = \frac{PL_0}{1 + C T^{\frac{3}{2}} \exp\left(-\frac{E_{defect}}{k_B T}\right)} \tag{16}$$

where PL$_0$ and C are positive fitting constants and E_{defect} is the defect energy relative to one of the band-edges. The factor $T^{\frac{3}{2}}$ accounts for the valence band density-of-states temperature-dependence [45].

Fig. 7 plots spectrally-integrated PL$_{defect}$ intensity versus the inverse thermal-energy (Arrhenius plot) for the three defects. We observe excellent fits for all the peaks, with correspondingly small errors in the extracted defect energy.

3.1.4. Intensity-dependent spectral PL (IDSPL)

Fig. 8 shows the IDSPL for the "Bright" and "Dark" locations measured at 80 K.

In the three cases, the peak emission energy for PL$_{defect}$ peak are observed to blue-shift with increasing excitation; this is a characteristic feature of DAP recombination [26] This is clearly demonstrated in Fig. 9, plotting the PL$_{defect}$ peak position ($h\nu_{peak}$) as a function of light intensity in Suns.

Further evidence to support the argument that PL$_{defect}$ is due to DAP recombination can be found by observing the excitation-dependence of the spectrally-integrated PL$_{defect}$, as shown in Fig. 10. The spectral-
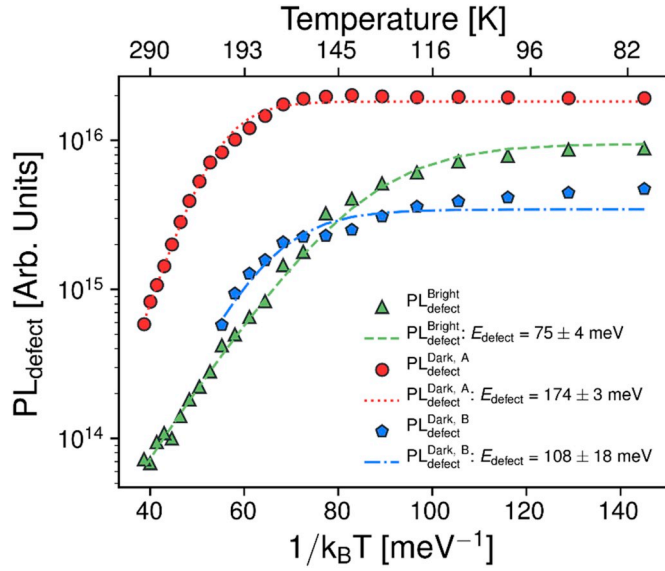
Fig. 7. Solid markers represent the measured data. Colored lines represent the best-fit according to Eq. (16). The extracted E_{defect} for each defect PL peaks, with standard errors are also indicated.

integral of each PL_{defect} peak is fitted against the light intensity using a power-law function of the form φ^k, where k is a positive constant (see Fig. 11). We observe for all peaks a sub-linear excitation dependence. Such an excitation-dependence is characteristic of e-A^0 (h-D^0) and D^0-A^0 recombination [23] However, based on the line-shape of the PL_{defect} we have already ruled out the possibility of PL_{defect} originating from e-A^0 (h-D^0) recombination; hence, DAP is the most likely mechanism .

3.1.5. Summary of the recombination mechanics
The initial analysis is summarized as follows:

1) *Symmetrical line-shape*: Recombination does not involve any free-carriers.
2) *Blue-shift with increasing excitation*: Characteristic specifically to D^0-A^0 recombination.
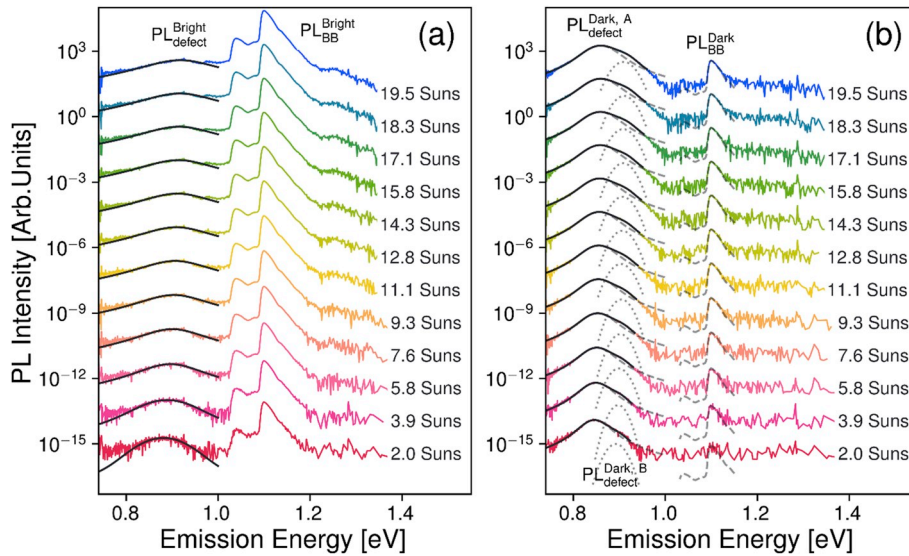
3) *Sub-linear excitation-dependence*: Characteristic to e-A^0 (h-D^0) and D^0-A^0 recombination.

Examining observations 1 to 3 above, only D^0-A^0 recombination is consistent. Therefore, the most likely mechanism responsible for the PL_{defect} is D^0-A^0 recombination.

3.2. Defect parameterization

In the previous section, DAP was identified as the most likely recombination mechanism for the investigated sample. In this section, we first introduce models for DAP recombination and then present a procedure to extract key defect parameters.

3.2.1. Theoretical model for DAP recombination
The steady-state DAP recombination rate was previously derived using the principle of detailed-balance [73] As each defect level in the pair may be ionized or unionized, treatment of the pair as a single defect leads to four charge state configurations: Both unoccupied (State 0), donor occupied (State 1'), acceptor occupied (State 1) and both occupied (State 2). The DAP recombination (R_{DAP}) is expressed as:
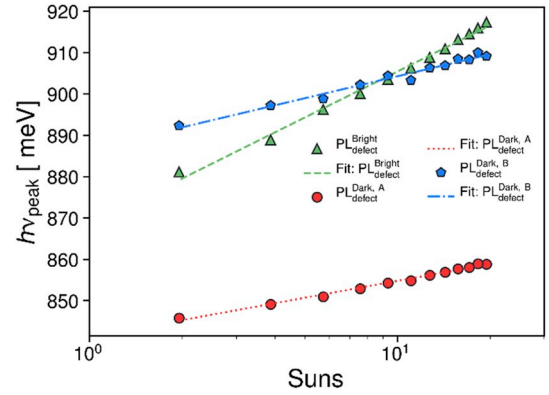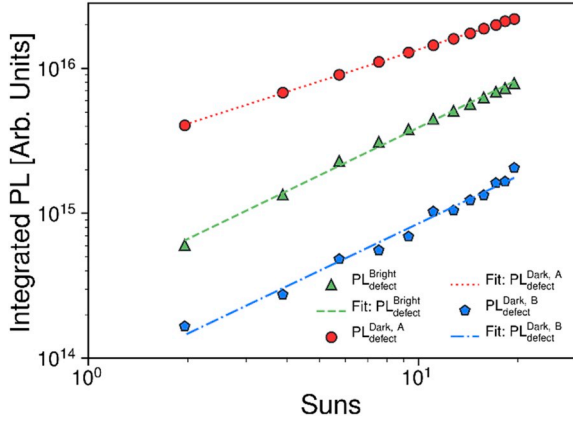

Fig. 9. $h\nu_{peak}$ versus Suns. The colored lines indicate a fit of the form: $A + \log_{10}(Suns)$ where A and B are positive constants.

Fig. 8. IDSPL for (a) Bright (b) Dark. All spectra are measured at a temperature of 80 K. Spectra are vertically offset for clarity. The fits for the PL_{defect} peaks and the peak emission energy for each peak are indicated also. For the "Dark" location, the PL_{BB} peaks from the "Bright" location are overlaid in dashed gray lines to indicate how the PL_{BB} peaks should appear, with lesser influence from the noise floor of the detector.

Fig. 10. Spectrally-integrated defect PL as a function of irradiance in Suns, for each defect PL peak. The data is represented by markers, and the fits are presented by the colored lines.

$$R_{\text{DAP}} = \frac{A}{B + C + D + E} N_t t^{'} \left(np - n_i^2 \right) \qquad 17$$

The terms A, B, C, D and E are:

$$A = \left(nC_{n0} + p_{\frac{1}{2}}C_{p1} \right) C_{n1}C_{p2} + \left(pC_{p2} + n_{\frac{3}{2}}C_{n1} \right) C_{n0}C_{p1} \qquad 18$$

$$B = \left(pC_{p2} + n_{\frac{3}{2}}C_{n1} \right) \left[\left(np + n_{\frac{1}{2}}^{'}p_{\frac{1}{2}}^{'} \right) C_{n0}C_{p1} + t^{'} pC_{p1} + n_{\frac{1}{2}}^{'}C_{n0}pC_{p1} \right] \qquad 19$$

$$C = \left(nC_{n0} + p_{\frac{1}{2}}C_{p1} \right) \left[\left(np + n_{\frac{3}{2}}p_{\frac{3}{2}}^{'} \right) C_{n1}C_{p2} + t^{'} nC_{n1} + p_{\frac{3}{2}}^{'}C_{p2}nC_{n1} \right] \qquad 20$$

$$D = t^{'} \left(nC_{n0} + p_{\frac{1}{2}}C_{p1} \right) \left(pC_{p2} + n_{\frac{3}{2}}C_{n1} \right) \qquad 21$$

$$E = nn_{\frac{1}{2}}^{'} \left(pC_{p2} + p_{\frac{1}{2}}C_{p1} \right) C_{n0}C_{n1} + pp_{\frac{3}{2}}^{'} \left(nC_{n0} + n_{\frac{3}{2}}C_{n1} \right) C_{p1}C_{p2} \qquad 22$$

Terms of the form C_{XY} are capture rates for carrier "X" for a pair in the charge state "Y". Capture rates are related to capture cross sections: $C_{XY} = v_{\text{th},X}\sigma_{XY}$ where $v_{\text{th},X}$ is the thermal velocity of carrier "X". N_t is the effective defect density, equal to $\min(N_d, N_a)$.

The terms $p_{3/2}^{'}$, $n_{1/2}^{'}$, $p_{1/2}$ and $n_{3/2}$ are defect-density terms (analogous to n_1 and p_1 in Shockley-Read Hall statistics):

$$p_{3/2}^{'} = \frac{N_V}{g_a} \exp\left(-\frac{E_a - E_v}{k_B T} \right) \qquad 23$$

$$n_{1/2}^{'} = \frac{N_C}{g_d} \exp\left(-\frac{E_c - E_d}{k_B T} \right) \qquad 24$$

$$n_{3/2} = \frac{N_C}{g_a} \exp\left(-\frac{E_a - E_{\text{Coulomb}} - E_v}{k_B T} \right) \qquad 25$$

$$p_{1/2} = \frac{N_V}{g_d} \exp\left(-\frac{E_c - E_d + E_{\text{Coulomb}}}{k_B T} \right) \qquad 26$$

where N_V and N_C are the effective density of states in the valence and conduction bands, respectively. g_D and g_A are the degeneracy factors, equal to 4 and 2 for donors and acceptors [74], respectively. $E_A - E_v$ and $E_c - E_d$ represent the position of the acceptor and donor energy levels above and below the valence and conduction band, respectively.

3.2.2. Theoretical model for DAP spectral line-shape

DAP recombination occurs due to carrier tunneling between a donor and acceptor and is therefore strongly dependent on their spatial separation. Assuming at least one of the defect levels is described by a hydrogen-like wave-function, the probability of recombination ($t^{'}$) of a single DAP is [73].

$$t^{'} = t_0 \exp\left(-\frac{2r}{a_{\text{Bohr}}} \right) \qquad 27$$

where r is the separation distance between the donor and acceptor in the pair, t_0 is the transition rate constant and a_{Bohr} is the Bohr radius of the shallower defect. The emitted photon energy is expressed as:
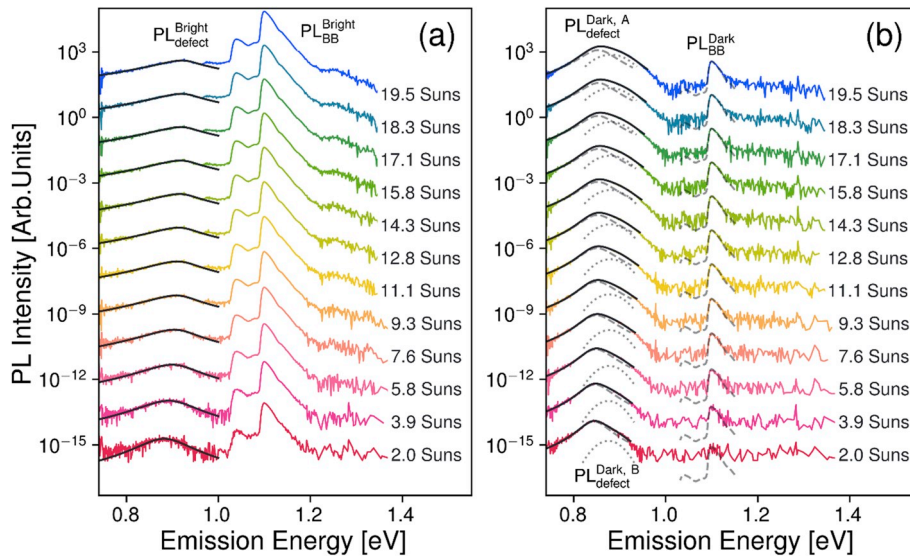
Fig. 11. Re-fitted IDSPL using the physical model (Eq. (31)) for the DAP spectral line-shape for (a) Bright (b) Dark.

$$hv_{\text{DAP}} = E_g - (E_a + E_d) + \frac{q^2}{\varepsilon_{\text{Si}}}\frac{1}{r} \qquad\qquad 28$$

where E_g is the band-gap energy, q is the electronic charge, ε_{Si} is the dielectric constant of silicon, and $E_a + E_d$ is the sum of the donor and acceptor energies. The last term accounts for the Coulombic interaction between donor and acceptor and is denoted as E_{Coulomb}.

The DAP spectral line-shape is a function of the Coulomb energy and takes the form [75].

$$PL_{\text{DAP}}(E_{\text{Coulomb}})\, dE \propto \left(\frac{E_d}{E_{\text{Coulomb}}}\right)^{-4} \exp\left(-4\frac{E_d}{E_{\text{Coulomb}}}\right) dE_{\text{Coulomb}} \qquad 29$$

Eq. (29) is valid for perfect compensation of donor and acceptor defects ($K = 1$):

$$K = \frac{N_a}{N_d} \qquad\qquad 30$$

where N_a and N_d are the acceptor and the donor defect concentrations, respectively.

For imperfect compensation, random electric fields exist due to the presence of ionized and non-ionized pairs in close proximity. These random fields are quenched by dielectric relaxation, leading to a broadening of the low-energy side of the DAP emission spectra. The DAP spectra is then described by [27].

$$PL_{\text{DAP}}(E) \propto \int_0^{+\infty} r \times t^{'} \times \frac{qF_{\text{md}}r^2}{(qF_{\text{md}}r)^2 + (E - E_{\text{Coulomb}})^2}\, dr \qquad 31$$

The term $F_{\text{md}} = 2.515 KqN_d^{2/3}/\varepsilon$ represents the most probable electric field. The subscript "md" stands for most-probable (m) and randomly oriented dipoles (d) [27].

3.2.3. Intensity-dependent spectral PL (IDSPL)

IDSPL determines two main parameters. First, the PL_{defect} peak emission energy is used to calculate the sum of donor and acceptor energies. Secondly, the spectrally-integrated PL_{defect} is used to estimate the effective defect density.

First, we present the re-fitted spectra of $PL_{\text{defect}}^{\text{Bright}}$, $PL_{\text{defect}}^{\text{Dark, A}}$ using the physical DAP spectral line-shape model (Eq. (21)–30). It was not possible to fit the shoulder peak $PL_{\text{defect}}^{\text{Dark, B}}$ using this model. Hence, this peak is fitted using the phenomenological Voight function [71] Further investigation may be required to explain this discrepancy. The defect-density related parameter $KN_d^{\frac{2}{3}}$, extracted from the fitted F_{md} value is on the order of 10^{11} cm^{-2}. This will be used later to estimate the concentrations of donor and acceptor defects.

3.2.4. Sum of donor and acceptor defect energies using the defect PL peak emission energy

We apply Eq. (28) to the peak PL_{defect} emission energy ($hv_{\text{DAP}}^{\text{peak}}$) using an average value for the DAP separation distance (r_{avg}). A plot of $E_g - hv_{\text{DAP}}^{\text{peak}}$ vs. $1/r_{\text{avg}}$ is a straight line with slope equal to $-q^2/4\pi\varepsilon_{\text{Si}}$ and y-intercept equal to $E_a + E_d$. r_{avg} is calculated using $\overline{\Delta n}$ [72] It is assumed that each photoexcited carrier has a sphere of influence with radius equal to $0.5 \times (\overline{\Delta n})^{-\frac{1}{3}}$. The average separation distance of a pair within this spherical volume is $2^{-\frac{1}{3}}$ of this radius [72] This yields the estimation of $r_{\text{avg}} \approx (16\Delta n)^{-\frac{1}{3}}$. To ensure the slope of the straight line is equal to $-q^2/4\pi\varepsilon_{\text{Si}}$, we consider a fitting factor β, so that r_{avg} is expressed as:

$$r_{\text{avg}} = \frac{1}{\beta} \times (16\Delta n)^{-\frac{1}{3}} \qquad\qquad 32$$

We emphasize that this fitting is only a reasonable assumption if the plot of $E_g - hv_{\text{DAP}}^{\text{peak}}$ vs. $(\overline{\Delta n})^{\frac{1}{3}}$ is a straight line with positive intercept and

negative slope.

Fig. 12 presents a plot of $E_g - hv_{\text{DAP}}^{\text{peak}}$ versus $1/r_{\text{avg}}$. For all three peaks, the trends are quite linear, supporting the estimation of r_{avg} using $\overline{\Delta n}$. Consequently, errors for the sum of defect energies are in the range of only a few meV. Note that these errors are calculated from the least-squares fit of the measured data. The error bars are the least square error for the PL_{defect} peak energy based on fitting the spectra.

The values of β are more than an order larger than unity. As the separation distance between photoexcited pairs is inversely proportional to β, this is interpreted to mean the average separation distance between donor-acceptor pairs is much smaller than the average distance between photoexcited carriers. Conversely, if β was equal to unity, it would imply each photoexcited carrier lies on a donor-acceptor pair. A $\beta < 1$ would imply that on average donor-acceptor pairs are much more sparse than the photoexcited carriers.

One possible explanation for $\beta > 1$ is that the defects are localized into clusters, so that the average distance between pairs in a cluster is much smaller than the average separation distance of the photoexcited carriers, which are assumed to be randomly distributed. Physically, this could be due to localized defects including dislocations and oxide precipitates.

3.3. Estimation of the effective defect density from the spectrally-integrated defect PL

The spectrally-integrated PL_{defect} is converted into a DAP recombination rate (R_{DAP}). This is approximated as the product of the effective DAP defect density (N_t) and the inter-level transition rate (W_0):

$$R_{\text{DAP}} = N_t \times W_0 \exp\left(-\frac{2r}{a_{\text{Bohr}}}\right) \qquad\qquad 33$$

This is a reasonable approximation under the following assumptions:

1) The defect density terms ($p_{32}^{'}, n_{12}^{'}, p_{12}, n_{32}$) are negligible compared to either n or p. This is a reasonable assumption at the low temperature of 80 K, as these terms have a Boltzmann temperature-dependence, which quenches at low temperature.
2) Terms containing $t^{'}$ in A, B, C, D, E may be neglected. This is justified as the DAP lifetimes are very large compared to the effective lifetime ($\frac{\tau_{\text{DAP}}}{\tau_{\text{eff}}} \approx \frac{10^{-1}}{10^{-5}} > 10^4$), meaning that the DAP recombination does not control the net recombination rate.

Substituting $r = r_{\text{avg}}$, a plot of R_{DAP} versus r_{avg} on a logarithmic-scaled y-axis should appear as a straight line with y-intercept of $N_t \times W_0$ and slope of $-2/a_{\text{Bohr}}$. Fig. 13 demonstrates good agreement between this model and the measured data, particularly for small r_{avg}. If W_0 is known, N_t may be determined. W_0 can be approximated by the expression [75].
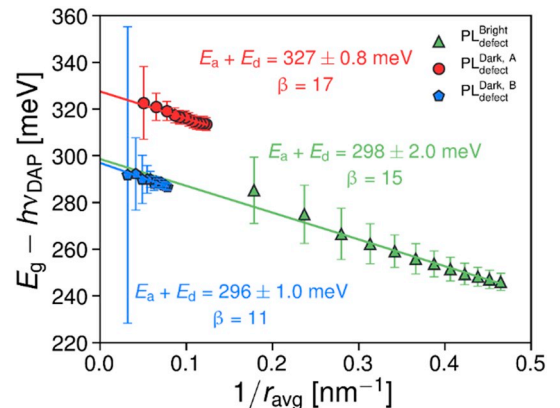
Fig. 12. $hv_{\text{DAP}}^{peak} - E_g$ versus $1/r_{\text{avg}}$. The defect sum $E_a + E_d$ and β are shown also.

$$W_0 = \frac{1.1 \times 10^{-43}}{r_1^5 a_\perp^2 a_\parallel}$$

34

where r_1 is the acceptor Bohr radius, $a_\perp$ and $a_\parallel$ are the transverse and longitudinal donor radii, respectively. The measured Bohr radii are on the order of $1 - 10$ nm, estimating W_0 in the order of $10^6 - 10^{12}$ s^{-1}. This corresponds to N_t in the order of $10^4 - 10^{11}$ cm^{-3}. Assuming $N_a > N_d$, the effective defect density is equal to N_d and using the previous result of $KN_d^{\frac{2}{3}} \sim 10^{11}$ cm^{-2}, N_a is estimated $10^{12} - 10^{15}$ cm^{-3}. This large spread in N_a is due to the high-sensitivity of W_0 to the Bohr radii. Time-resolved DAP PL studies are a candidate method to experimentally determine W_0 [76].

3.3.1. Temperature-dependent spectral PL (TDSPL)

TDSPL were used to determine E_a and to estimate E_d. First, the spectra were re-fitted using the physical model for the DAP spectral line-shape, as shown in Fig. 14.

The spectrally-integrated PL for each DAP peak were converted into DAP recombination rates and then DAP lifetimes as per Section C (*Calibrating the band-to-band PL to average excess carrier densities*). We used the previously established physical model for R_{DAP} to fit the data. Considering the temperature-dependence of the capture cross-sections, various combinations of multi-phonon emission, cascade capture and excitonic Auger mechanisms were tested [77] The quality of the fit was not improved, with the fit being mostly sensitive to E_a. Therefore, we assumed temperature-independent capture-cross sections in the following fitting procedure.

Fig. 15 plots the DAP lifetime as a function of $1/k_BT$. Note that the large values of the DAP lifetime are not unreasonable given that the total DAP recombination is small compared to the total recombination (generation) rate. The extracted E_a have reasonable error, but the errors on E_d are gross. Interestingly, the defect sum agrees reasonably well with those determined from IDSPL.

3.3.2 Summary of results

Table 2 summarises the results of the analyses, comparing E_a, E_d and $E_a + E_d$. The phenomenological TDSPL model fits the data well and extracts E_a with a small error. The theoretical TDSPL model gives both E_a and E_d; the error on E_a is generally reasonable, but the error on E_d is gross. This is interpreted to mean the TDSPL data is much more sensitive to E_a than E_d. Interestingly, the acceptor energies for both methods agree. Hence, we suggest that the phenomenological model can be used to estimate E_a. This consistency, despite the injection-independence of the phenomenological model for DAP recombination, implies that the temperature-dependence is much stronger than the injection-dependence. IDSPL gives $E_a + E_d$, with very small error. Surprisingly, the sum of defect energies using the physical TDSPL model is remarkably
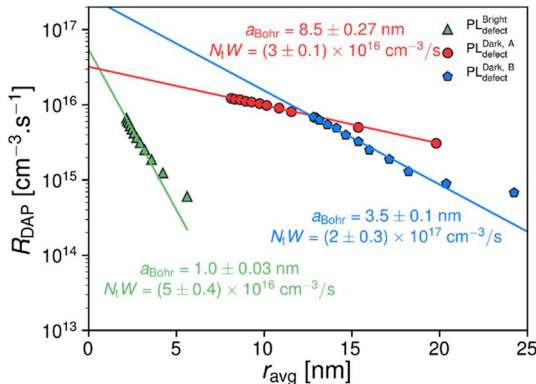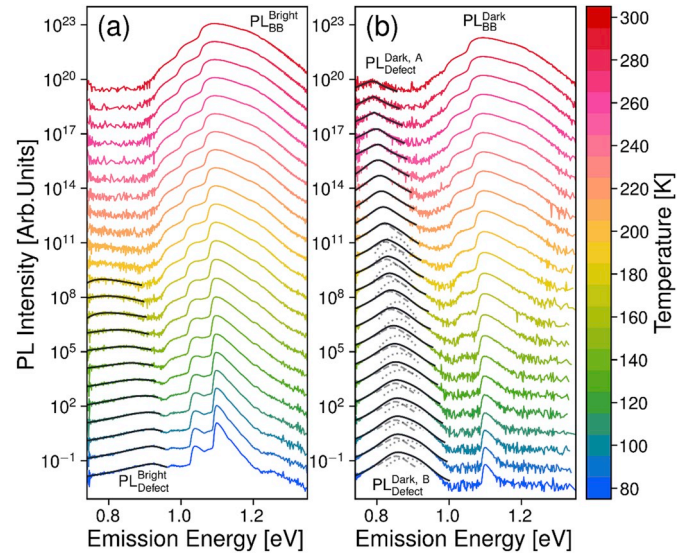

Fig. 14. TDSPL refitted using physical DAP Spectra line-shape model for (a) Bright and (b) Dark locations. All spectra are measured at a light intensity of 19.5 Suns.
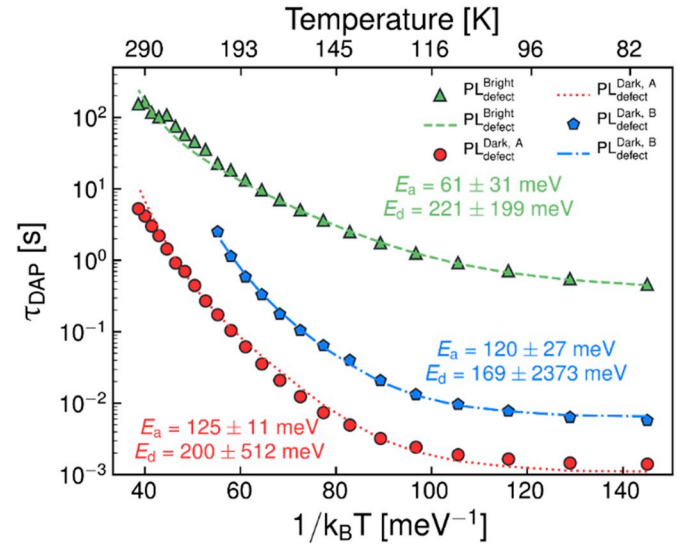

Fig. 15. τ_{DAP} versus $1/k_BT$. The colored lines are the fits using the physical model for DAP recombination (Eq. (17) – 26). Extracted E_a and E_d are shown also.

close to this result (15–26 meV) despite the gross error in E_d.

Fig. 16 is a band diagram summarizing E_a from the physical TDSPL model and E_d from the physical IDSPL model. We chose the results of the physical models over the simple models despite the larger errors because they are based on well-established theories rather than an empirical relationship. Note that in all cases, the acceptor energies are "shallow" with respect to the "deep" donor energies; this is consistent with DAP recombination in an *n*-type semiconductor. For the "Dark" location, E_a are within the same range for both PL$_{defect}^{Dark, A}$ and PL$_{defect}^{Dark, B}$ defect PL peaks, indicating that that they may share the same acceptor defect level. The difference in PL peak energies can be explained by E_d, which is approximately 25 meV smaller for PL$_{defect}^{Dark, B}$ than PL$_{defect}^{Dark, A}$. For the "Bright" location, E_a is significantly smaller (30 meV) and E_d is significantly larger (25 meV) compared to respective values in the "Dark" location. This may imply that the defect PL in the "Bright" location has a different origin than the defect PL in the "Dark" location.

Fig. 13. DAP recombination rate as a function of r_{avg}. Extracted a_{Bohr} and N_tW_0 are shown also.

Table 2
Comparison of extracted defect energies combining both TDSPL and IDSPL data.

	TDSPL (Phenomological)	TDSPL (Physical)			IDSPL (Physical)	IDSPL (Physical) + TDSPL (Physical)	IDSPL (Physical) + TDSPL (Phenomological)
	E_a [meV]	E_a [meV]	E_d [meV]	$E_a + E_d$ [meV]	$E_a + E_d$ [meV]	E_d [meV]	E_d [meV]
Dark, A	174 ± 4	125 ± 11	221 ± 199	346 ± 199	327 ± 0.8	202 ± 11	153 ± 4.1
Dark, B	108 ± 18	120 ± 27	169 ± 2373	289 ± 2373	296 ± 1.0	176 ± 27	188 ± 18
Bright	75 ± 4	61 ± 31	221 ± 199	282 ± 201	298 ± 2.0	237 ± 31	223 ± 4.5
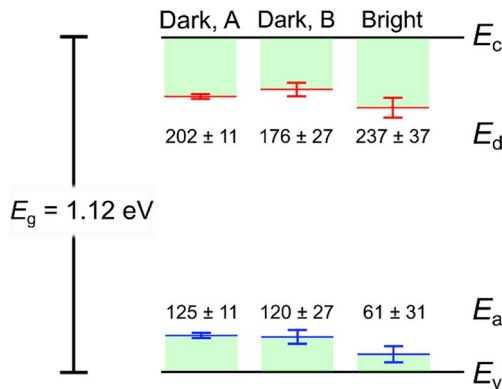
Fig. 16. *Band diagram showing the extracted defect energies (E_a and E_d). E_V and E_C represent the valence and conduction band-edges, respectively. The long horizontal lines represent the position of the defect energies and the short bars represent the standard error-bars. All values of the defect energies are in units of meV.*

4. Conclusions

This study presented a novel method to quantitatively analyze PL_{defect} in silicon. The method is based on temperature and intensity-dependent spectral PL measurements and consists of a "coarse" analysis, followed by a "detailed" analysis step. The "coarse" analysis is used to determine the type of radiative defect recombination mechanism by fitting the data according to simple phenomenological models. In the second step, the defect recombination is studied in more detail given that physical models for the specific radiative defect recombination identified in the "coarse" step are known. To assist this step, methods to determine Δn from the spectra are also established. This is based on fitting the measured PL_{BB} spectra according to the spectra predicted by modelling photon reabsorption.

To implement this method, we selected particular *n*-type mono-crystalline silicon samples. These samples were thermally processed to activate non-uniform bulk defects known to produce defect luminescence. Due to the high non-uniformity in the defect concentration we selected a high and low-lifetime region for spectral measurements. The "coarse" analysis step revealed donor-acceptor pair as the radiative defect recombination mechanism. In the "detailed" analysis step, the energy levels of both the acceptor and donor-defects were extracted. We emphasize that because we obtain these values directly from the defect luminescence, our method provides higher confidence than more traditional indirect methods, such as those involving PL_{BB} and photoconductance.

A limitation of this method is the large number of spectra required. This may be partially compensated for considering the large amount of information that may be obtained from these measurements.

Author contributions

Robert (μRob) **Lee Chin**: Conceived and designed the analysis;

Collected the data; Contributed data or analysis tools; Performed the analysis; Wrote the paper; **Michael Pollard**; Contributed data or analysis tools; Other contribution; **Yan Zhu**: Contributed data or analysis tools; Other contribution; **Ziv Hameri:** Contributed data or analysis tools; Other contribution

References

[1] G. Davies, Phys. Rep. 176 (1989) 83.
[2] W. Bludau, A. Onton, W. Heinke, J. Appl. Phys. 45 (1974) 1846.
[3] G.G. Marfarlane, T.P. Mclean, J.E. Quarrington, V. Roberts, Phys. Rev. 111 (1958) 1245.
[4] I. Pelant, J. Valenta, Luminescence Spectroscopy of Semiconductors, Oxford University Press, 2013.
[5] R.C. Newman, Rep. Prog. Phys. 45 (1982) 1163.
[6] W. Shockley, W.T. Read, Phys. Rev. 87 (1952) 835.
[7] R.N. Hall, Phys. Rev. 87 (1952) 387.
[8] T. Trupke, P. Wuerfel, S.W. Glunz, Appl. Phys. Lett. 92 (2008) 222112.
[9] S. Pizzini, E. Leoni, S. Binetti, M. Acciarri, A. Le Donne, B. Pichaud, Solid State Phenom. 95–96 (2004) 273.
[10] R. Sauer, J. Weber, J. Stolz, E.R. Weber, K.H. Küsters, H. Alexander, Appl. Phys. A 36 (1985) 1.
[11] I. Tarasov, S. Ostapenko, C. Haessler, E.-U. Reisner, Mater. Sci. Eng. B 71 (2000) 51.
[12] K. Bothe, R.J. Falster, J.D. Murphy, Appl. Phys. Lett. 101 (2012), 032107.
[13] H.T. Nguyen, F.E. Rougieux, F. Wang, D. Macdonald, Energy Procedia 77 (2015) 619–625.
[14] S. Pizzini, M. Guzzi, E. Grillit, G. Borionetti, E. Grilli, G. Borionetti, J. Phys. Condens. Matter 12 (2000) 10131.
[15] S. Binetti, S. Pizzini, E. Leoni, R. Somaschini, A. Castaldini, A. Cavallini, J. Appl. Phys. 92 (2002) 2437.
[16] S. Binetti, A. Le Donne, A. Sassella, Sol. Energy Mater. Sol. Cells 130 (2014) 696.
[17] R. Lee Chin, Y. Zhu, G. Coletti, S. Binetti, M. Pollard, Z. Hameiri, in: 7th World Conf, 2018, pp. 2524–2527.
[18] K. Bothe, S. Herlufsen, J.D. Murphy, Semicond. Sci. Technol. 34 (2019), 035030.
[19] M. Tajima, Y. Iwata, F. Okayama, H. Toyota, H. Onodera, T. Sekiguchi, J. Appl. Phys. 111 (2012) 113523.
[20] S. Binetti, R. Somaschini, A. Le Donne, E. Leoni, S. Pizzini, D. Li, D. Yang, J. Phys. Condens. Matter 14 (2002) 13247.
[21] S. Pizzini, M. Acciarri, E. Leoni, A. Le Donne, Phys. Status Solidi B 222 (2000) 141.
[22] E. Leoni, L. Martinelli, S. Binetti, G. Borionetti, S. Pizzini, J. Electrochem. Soc. 151 (2004) G866.
[23] T. Schmidt, K. Lischka, W. Zulehner, Phys. Rev. B 45 (1992) 8989.
[24] M. Tajima, K. Tanaka, S. Dubois, J. Veirman, K. Nakagawa, A. Ogura, Jpn. J. Appl. Phys. 54 (2015) 111304.
[25] B.K. Meyer, J. Sann, S. Lautenschläger, M.R. Wagner, A. Hoffmann, Phys. Rev. B 76 (2007) 184120.
[26] W.E. Hagston, J. Lumin. 3 (1971) 253.
[27] N.A. Bogoslovskiy, P. V Petrov, N.S. Averkiev, J. Low Temp. Phys. 45 (2019) 146.
[28] D.G. Thomas, J.J. Hopfield, W.M. Augustyniak, Phys. Rev. 140 (1965) 202.
[29] M. Tajima, T. Iwai, H. Toyota, S. Binetti, D. MacDonald, J. Appl. Phys. 110 (2011), 043506.
[30] H.T. Nguyen, Y. Han, M. Ernst, A. Fell, E. Franklin, D. MacDonald, Appl. Phys. Lett. 107 (2015), 022101.
[31] H.T. Nguyen, D. Yan, F. Wang, P. Zheng, Y. Han, D. Macdonald, Phys. Status Solidi Rapid Res. Lett. 9 (2015) 230.

[32] P. Gundel, M.C. Schubert, W. Kwapil, J. Schön, M. Reiche, H. Savin, M. Yli-Koski, J. A. Sans, G. Martinez-Criado, W. Seifert, W. Warta, E.R. Weber, Phys. Status Solidi Rapid Res. Lett. 3 (2009) 230.
[33] H.T. Nguyen, M.A. Jensen, L. Li, C. Samundsett, H.C. Sio, B. Lai, T. Buonassisi, D. Macdonald, IEEE J. Photovoltaics 7 (2017) 772.
[34] F.D. Heinz, W. Warta, M.C. Schubert, Sol. Energy Mater. Sol. Cells 158 (2016) 107.
[35] H.T. Nguyen, F.E. Rougieux, F. Wang, H. Tan, D. Macdonald, IEEE J. Photovoltaics 5 (2015) 799.
[36] M. Inoue, H. Sugimoto, M. Tajima, Y. Ohshita, A. Ogura, J. Mater. Sci. Mater. Electron. 19 (2008) 132.
[37] F.D. Heinz, M. Kasemann, W. Warta, M.C. Schubert, Appl. Phys. Lett. 107 (2015) 122101.
[38] A. Roigé, J. Alvarez, A. Jaffré, T. Desrues, D. Muñoz, I. Martín, R. Alcubilla, J.-P. Kleider, J. Appl. Phys. 121 (2017), 063101.
[39] J.A. Giesecke, B. Michl, F. Schindler, M.C. Schubert, W. Warta, Sol. Energy Mater. Sol. Cells 95 (2011) 1979.
[40] R.A. Sinton, A. Cuevas, M. Stuck, in: 25th IEEE Photovolt. Spec. Conf, 1996, pp. 457–460.
[41] N.E. Grant, V.P. Markevich, J. Mullins, A.R. Peaker, F. Rougieux, D. Macdonald, Phys. Status Solidi Rapid Res. Lett. 10 (2016) 443.
[42] M. Tajima, M. Ikebe, Y. Ohshita, A. Ogura, J. Electron. Mater. 39 (2010) 747.
[43] T. McHedlidze, W. Seifert, M. Kittler, A.T. Blumenau, B. Birkmann, T. Mono, M. Müller, J. Appl. Phys. 111 (2012), 073504.
[44] F.D. Heinz, Microscopic Photoluminescence Spectroscopy on Silicon, PhD Thesis, Fraunhofer Institute for Solar Energy Systems, 2015.
[45] M. Suezawa, Y. Sasaki, K. Sumino, Phys. Status Solidi A 79 (1983) 173.
[46] A. Le Donne, S. Binetti, V. Folegatti, G. Coletti, Appl. Phys. Lett. 109 (2016), 033907.
[47] D.N.R. Payne, M.K. Juhl, M.E. Pollard, A. Teal, D.M. Bagnall, in: 43rd IEEE Photovolt. Spec. Conf, 2016, pp. 1585–1589.
[48] H.T. Nguyen, F.E. Rougieux, F. Wang, H. Tan, D. Macdonald, IEEE J. Photovoltaics 5 (2015) 799.
[49] J. Mooney, P. Kambhampati, J. Phys. Chem. Lett. 4 (2013) 3316.
[50] D. Macdonald, A. Liu, H.T. Nguyen, S.Y. Lim, F.E. Rougieux, in: 31st Eur. Photovolt. Sol. Energy Conf. Exhib, 2015, pp. 440–443.
[51] F. Wolny, A. Krause, A. Oehlke, M. Wagner, Energy Procedia 92 (2016) 274.
[52] W. Kern, J. Electrochem. Soc. 137 (1990) 1887.

[53] Z. Hameiri, N. Borojevic, L. Mai, N. Nandakumar, K. Kim, S. Winderbaum, IEEE J. Photovoltaics 7 (2017) 996.
[54] V.G. Bauer, Ann. Phys. 5 (1934) 434.
[55] T. Trupke, R.A. Bardos, M.D. Abbott, Appl. Phys. Lett. 87 (2005) 184102.
[56] T. Trupke, M.A. Green, P. Würfel, P.P. Altermatt, A. Wang, J. Zhao, R. Corkish, J. Appl. Phys. 94 (2003) 4930.
[57] P.P. Altermatt, F. Geelhaar, T. Trupke, X. Dai, A. Neisser, E. Daub, in: Proc. 5th Int. Conf. Numer. Simul. Optoelectron. Devices, 2005, pp. 47–48.
[58] M. Rüdiger, T. Trupke, P. Würfel, T. Roth, S.W. Glunz, Appl. Phys. Lett. 92 (2008) 222112.
[59] T. Trupke, J. Appl. Phys. 100 (2007), 063531.
[60] P. Wurfel, J. Phys. C Solid State Phys. 15 (1982) 3967.
[61] H.T. Nguyen, F.E. Rougieux, B. Mitchell, D. Macdonald, J. Appl. Phys. 115 (2014), 043710.
[62] J. Wen, L. Jia, Y. Zhu, Proc. of SPIE 7511 (2009) 751112.
[63] P.P. Altermatt, A. Schenk, G. Heiser, J. Appl. Phys. 100 (2016) 113714.
[64] J. Haunschild, I.E. Reis, J. Geilker, S. Rein, Phys. Status Solidi Rapid Res. Lett. 5 (2011) 199.
[65] Y. Zhu, F. Rougieux, N. Grant, J. Mullins, J.A. De Guzman, J.D. Murphy, V. P. Markevich, G. Coletti, A.R. Peaker, Z. Hameiri, in: AIP Conf. Proc, 2019, p. 140014.
[66] J.D. Murphy, K. Bothe, M. Olmo, V.V. Voronkov, R.J. Falster, J. Appl. Phys. 110 (2011), 053713.
[67] J.D. Murphy, K. Bothe, R. Krain, V.V. Voronkov, R.J. Falster, J. Appl. Phys. 111 (2012) 113709.
[68] J.D. Murphy, M. Al-Amin, K. Bothe, M. Olmo, V.V. Voronkov, R.J. Falster, J. Appl. Phys. 118 (2015) 215706.
[69] J.D. Murphy, R.E. McGuire, K. Bothe, V.V. Voronkov, R.J. Falster, Sol. Energy Mater. Sol. Cells 120 (2014) 402.
[70] W.S. Liang, K.J. Weber, Y.L. Ren, Prog. Photovoltaics 21 (2013) 1640.
[71] B.H. Armstrong, J. Quant. Spectrosc. Radiat. Transf. 7 (1967) 61.
[72] T.H. Gfroerer, C.E. Gillespie, J.P. Campbell, M.W. Wanlass, J. Appl. Phys. 98 (2005), 093708.
[73] L.W. Aukerman, M.F. Millea, Phys. Rev. 148 (1966) 759.
[74] R.B. Dingle, The london, edinburgh, and dublin philos, Mag. J. Sci. 46 (1955) 831.
[75] F. Williams, R. Hill, Phys. Rev. 177 (1967) 1182.
[76] Ch Fricke, J. Cryst. Growth 138 (1994) 815.
[77] F.E. Rougieux, C. Sun, D. Macdonald, Sol. Energy Mater. Sol. Cells 187 (2018) 263.